Article:
Olerni, C, Jia, J and Wang, M (2013) Measurement of air distribution and void fraction of an upwards air-water flow using electrical resistance tomography and a wire-mesh sensor. Measurement Science and Technology, 24 (3). ARTN 035403. ISSN 0957-0233

https://doi.org/10.1088/0957-0233/24/3/035403

Measurement of Air Distribution and Void Fraction of an Upwards Air-water Flow Using Electrical Resistance Tomography and Wire-mesh Sensor

Claudio Olerni, Jiabin Jia* and Mi Wang

School of Process, Environmental and Materials Engineering, University of Leeds, Leeds, LS2 9JT, UK

E-mail: pm09co@leeds.ac.uk, prejj@leeds.ac.uk, m.wang@leeds.ac.uk

* Corresponding Author. Tel.: 0113 3432357; Fax: +44 (0) 113 343 2435

Abstract

The measurements on an upwards air-water flow simultaneously obtained with a dual-plane Electrical Resistance Tomography (ERT) and a Wire-Mesh Sensor (WMS) are reported. The ultimate measurement target of both ERT and WMS is the same, the electrical conductivity of the medium. The ERT is a non-intrusive device whereas the WMS requires a net of wires which physically crosses the flow. This paper presents comparisons between the results simultaneously obtained from the ERT and the WMS for evaluation and calibration of the ERT. The length of vertical testing pipeline section is 3 meters with an internal diameter of 50 mm. Two distinct sets of air-water flow rate scenarios, bubble and slug regimes, were produced in the experiments respectively. The Fast Impedance Camera (FICA) ERT recorded the data at an approximated time resolution of 896 frames per second (fps) per plane in contrast with the 1024 fps of the wire-mesh sensor WMS200. The set-up of the experiment was based on the well established knowledge on air-water upwards flow, particularly, the specific flow regimes and wall peak effects. The local air void fraction profiles and the overall air void fraction were produced from two systems to establish a consistent comparison of the data accuracy. The conventional bulk flow measurements in air mass and electromagnetic flow metering, as well as pressure and temperature were employed, which brought the necessary calibration to the flow measurements. The results show the profiles generated from two systems have a level of inconsistency, particularly in a wall peak and a core peak from the ERT and WMS respectively. Whereas the two tomography instruments achieve a good agreement on the overall air void fraction for the bubble flow. For the slug flow, when the void fraction is over 30%, the ERT underestimates the void fraction, however a linear relation between ERT and WMS is still observed.

Keywords: Electrical Resistance Tomography, Wire-mesh Sensor, Upwards air-water flow measurements, Local air void fraction profile

1. Introduction

1.1. Air void fraction in upwards air-water flows

Metering of air distribution and void fraction in the air-water flows has been investigated since the early 60s. Malnes [1] depicted the local void fraction profiles in the bubble flow pattern. Figure 1 illustrates his findings. The local air void fractions have different radial distribution in respect to the superficial gas velocities.

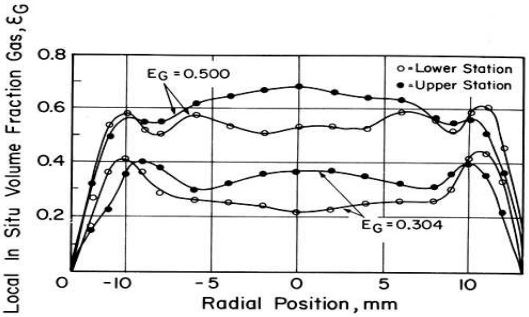

Figure 1: Typical concentration profiles in the bubble flow pattern [1] (Reprinted with permission from Institute for Atomenergi, Kjeller Research Establishment).

Serizawa and Katoaka [2] were also the former to study the lateral gas void fraction distribution (in some papers referred to concentration distribtuion) in a vertical pipe. Figure 2 schematically plots four main air void fraction patterns in the bubble flow regime. They discovered the gas void fraction profile pattern depends on both gas volumetric flow rate and liquid volumetric flow rate. The wall peak pattern occurs if more gas distributes closely to the pipe wall. The profile pattern gradually develops to the intermediate peak and the slug peak as the gas volumetric flux increases. Finally, more gas gathers towards the central pipe and the core peak pattern shows.

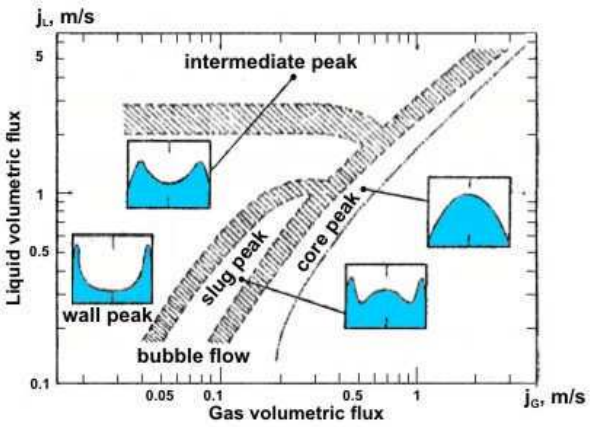

Figure 2: Lateral Void distribution patterns for air-water flow in vertical pipe [2] (Reprinted with permission from Isao KATAOKA, Osaka University).

Wang *et al.* [3] extracted similar results from the air distribution in bubbly two-phase flows. In additions, they noticed the wall peak pattern appeared for upwards flows, conversely to the downwards flows that exhibited a core peak pattern. Consequently, the work of Liu *et al.* [4] brought a better understanding on these phenomena. It resulted in that bubble size and shape affected the air volume fraction distribution and it was particularly true at low liquid flow rates. This concept was further consolidated by Leahey [5] when he analysed the phase separation and phase distribution to predict the multidimensional behaviour using two-phase models. Two years later, Serizawa *et al.* [6] reiterated Leahey's and Liu's conclusions. They found evidences that large bubbles tended to move towards the core of the pipe, whereas, the small spherical bubbles are more likely to be next to the pipe wall. The local air void fraction profiles with different patterns are shown in Figure 3.

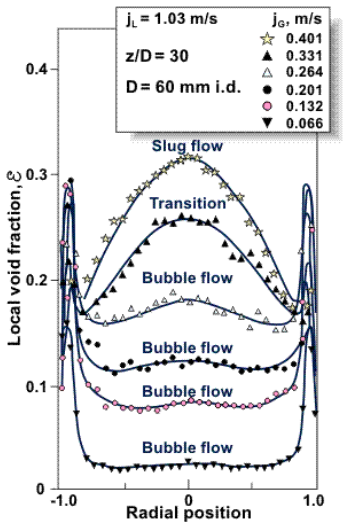

Figure 3: Air void distribution models in vertical upwards flow pipe [6] (Reprinted with permission from Isao Katoaka, Osaka University).

Later on these years, several other mechanism and factors influencing bubble deposition and hence air void distribution have been revealed. These might be summarised as: bubble segregation due to a lateral lift force acting on bubbles; unequal pressure distribution provoked by non-uniform turbulence regions [7]; a force similar to diffusion force related to void fraction gradient; bubble coalescence, frequently referred to the *k-ε* model [7] and Reynolds stress mode [8] and the effect of bubble entrapment due to eddies formation. In a companion paper, Liu and Bankoff [4] proposed that the wall peak was generated by bubbles contact with the wall which was held against the latter due to the induction of surface tension forces. The drag forces caused by viscous effects stagnated bubbles at wall, which produced

a rotational and rolling movement along the internal surface of the channel.

1.2. Wire-mesh sensor for air concentration distribution comparison

Wire-Mesh Sensor (WMS) was successfully used for upwards gas-water flow measurement and validation [9], which measures the local electrical conductivity distribution of the fluids from the crossing points of two groups of perpendicular wires.

A comparison between 16×16 wire-mesh sensor and ultra-fast X-ray CT was carried out by Prasser *et al.* [10]. The experiments were performed at the ambient pressure and temperature with different air-water flow rates in a vertical pipe with 42 mm diameter. A sintered plate with a pore size of 100 µm and orifices of 5 mm were employed to produce bubble flow conditions. Figure 4 shows the part of outcomes with regards to air void fraction distribution. The radial void fraction profiles from two modalities are not completely consistent but have the similar tendency.

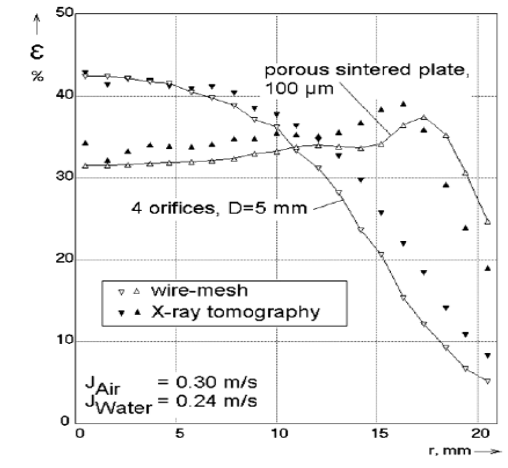

(a)

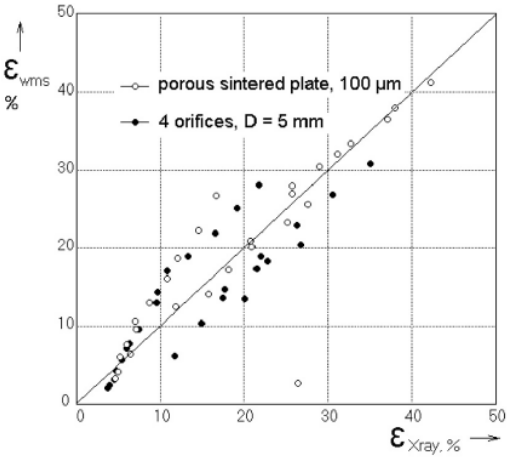

(b)

Figure 4: (a) Comparison of radial void fraction profiles. (b) Cross-sectional averaged void fractions between X-ray tomography data and wire-mesh sensor [10] (Reprinted with permission from Elsevier).

The investigation revealed that there was a good agreement between the void fractions metered by both the WMS and the ultra-fast X-ray scanner. However, large Taylor bubbles could not been perfectly detected by the mesh sensor itself. This corroborated the findings of Prasser *et al*. who noticed the generation of water films within the crossing wire points of the planes that detected an incorrect electrical conductivity for pure air [11].

Azzopardi *et al*. [12] found an excellent agreement of cross-sectional averaged void fractions between an Electrical Capacitance Tomography (ECT) and wire-mesh sensor output for an air/silicone oil flow in a vertical pipe. Figure 5 reports the comparison.

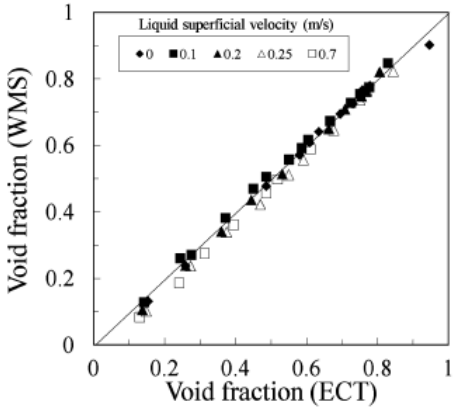

Figure 5: Comparison of overall averaged void fraction from ECT and WMS [11] (Reprinted with permission from Copyright Clearance Centre).

1.3. Scope of the study

Electrical Resistance Tomography (ERT) is able to measure the local distributions of the concentration and velocity of the dispersed phase inside conductive continuous phase. In this study, two flow regimes, bubble and slug, were created in the flow loop under several flow rate scenarios. These covered flow conditions either at constant superficial air velocity (Vsa) and variable superficial water velocity (Vsw) or at constant Vsw and variable Vsa. The measurements on the upwards concurrent air-water flow section were taken simultaneously by ERT and WMS. The radial air void fraction profiles and overall void fractions were extrapolated from the data process software of ERT and WMS. Then the results from two modalities were analysed and compared.

2. Experimental method

The existent experimental flow loop facility at University of Leeds was adapted to carry out the ex in flo wa m re

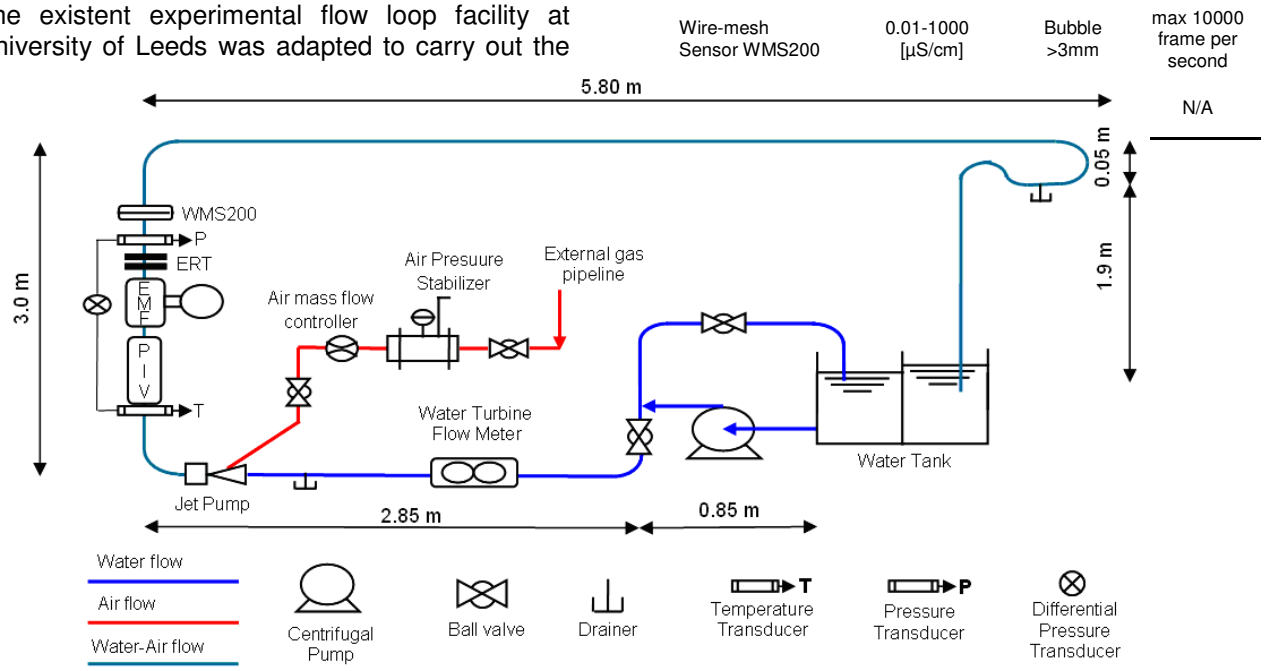

Figure 6: Sketch of the experimental flow loop.

The stabilised air flow rate is regulated by the air mass flow controller. After the loop bend, the upwards air-water mixture goes through the flow instrumentations, horizontal section and then back to the water tank, where air is released and water is recycled. The brief specifications of the flow instrumentations involved in the experiments are listed in Table 1.

Table 1: Specification of instrumentations in the flow loop.

Instrument	Measurement range	Accuracy	Time definition
Centrifugal single-phase pump	N/A	N/A	N/A
Water turbine flow meter (WTF)	0.00015- 0.0114 [m³/sec]	±1% FS	N/A
Air mass flow controller	0-100 [l/min]	±1.5% FS	N/A
Platinum RTD Temperature sensor	0-100 [ºC]	±0.25% FS	N/A
Electromagnetic Flow meter (EMF)	±12 [m/s]	± 0.2% of MV + 1 mm/s	N/A
Differential Pressure Sensor (DP)	±0.5 [Psid]	±0.25% FS	N/A
ERT	N/A	Bubble ≥5% $Ø_i$ tube	N/A
FICA software	N/A	Bubble ≥5% $Ø_i$ tube	1000 dual frame per second

2.1. Vertical upward flow section

The WMS200 exhibited a spatial resolution down to 3 mm [13], this represented the free space area situated at each plane between the 16x16 stainless steel electrodes (transmitters x receivers) network, arranged orthogonally to each other. The distance within the planes themselves was of 20 mm. The dual-plane ERT system displayed a longitudinal separation of 50 mm from plane 1 to plane 2, whereas, 16 stainless steel electrodes were equally mounted around the axial circumference of each sensor.

In order to ensure a high consistency of the readings between the ERT and the WMS200, two measurement modalities were positioned with a distance of approximately 0.25m (refer to Figure 7 for detailed dimensions). Because the WMS is an intrusive measurement device, it has to be located after ERT sensor to avoid its potential disturbance on flow patterns. A differential pressure transducer (DP), an absolute pressure sensor PXM209 and a Platinum RTD Temperature transducer were installed respectively to monitor the flow conditions.

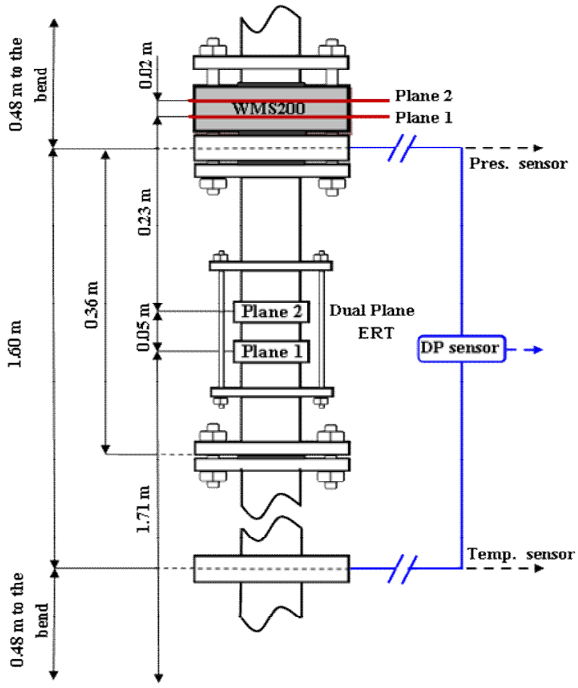

Figure 7: Sketch of the flow instrumentations at the University of Leeds.

2.2. Air-water two phase flow investigation

The air-water two phase flow was generated by injecting air into the liquid phase (tap water), both at the room temperature, through a jet pump connected to the flow loop (see Figure 6). The water flow rate was regulated manually by means of a ball valve and eventually recorded via a water turbine flow meter in revolutions per minute (RPM). The water turbine flow meter (WTF) was calibrated by an electromagnetic flow meter (EMF) to take the measurements of the volumetric water flow, Q_w, in m^3/h. Due to the EMF was located upstream of the air inlet, it was solely able to accomplish readings of the water flow. Conversely, the WTF positioned downstream before air injection was capable to acquire the interested liquid phase data. Equation (1) expresses the correlation between the EMF and WTF as shown below:

$$Q_w = 0.0469 \times RPM + 0.542 \quad (1)$$

The volumetric flow rate of air was easily determined via the air mass flow controller in standard liter per minute (SLPM) and consequently converted in m^3/h. The Changes of pressure and temperature were recorded and then considered to bring the necessary accuracy to the conversion. Subsequently, the superficial velocities of air and water, V_{sa} and V_{sw} respectively, were then extrapolated considering the 50 mm internal diameter of the pipe.

2.2.1. Generating data via ERT system

Figure 8 depicts a schematic of the Electrical Resistance Tomography measurement and the procedure to extract the targeted data from the ITS 2000 [14] and AIMFlow software [15]. The speed of the FICA ERT system [16] was configured as 896 frames per second. 7500 frames were specified to acquire, which took approximate 8 seconds. Additional 3 seconds were spent to transfer data from ERT system to the host PC.

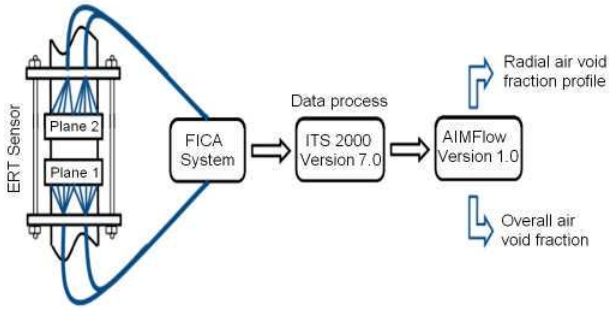

Figure 8: Schematic of the ERT measurement.

The DSP based FICA ERT system is a parallel data acquisition. It is able to sense dual ERT sensor planes synchronously using the adjacent sensing strategy. The responding voltages on the ERT electrodes were taken as reference when the flow loop was filled with the pure continuous phase only, then the responding voltages were measured again by ERT system when the air-water flow was running in the loop. The relative voltages difference from the continuous flow and two-phase flow were used to calculate the local conductivity on each pixel cross the electrode plane. The conversion from the relative voltages to conductivity was derived from the modified sensitivity coefficient back-projection algorithm (SBP) [14]. The volumetric void fraction of the dispersed phase (air) on each pixel, α, was then determined by the Maxwell relationship [17]. This was considered since it took in account of non-miscible phases, as the experiment scenario. Equation (2) describes it as:

$$\alpha = \frac{2\sigma_1 + \sigma_2 - 2\sigma_{mc} - \frac{\sigma_{mc}\sigma_2}{\sigma_1}}{\sigma_{mc} - \frac{\sigma_2}{\sigma_1}\sigma_{mc} + 2(\sigma_1 - \sigma_2)} \quad (2)$$

The conductivity of air phase is regarded as zero ($\sigma_2 = 0$) so that Equation (2) is further simplified as Equation (3).

$$\alpha = \frac{2\sigma_1 - 2\alpha_{mc}}{\sigma_{mc} + 2\sigma_1} \quad (3)$$

Where, σ_1 represented the conductivity of the continuous phase (the conductivity of water in the test is 0.39 mS/cm) and σ_{mc} was the tomography reconstructed measured local conductivity in mS/cm [14]. The overall air void fraction α_{air} is deduced from the average of the pixel void fraction.

2.2.2. Generating data via WMS200 system

Figure 9 depicts the schematic of the wire-mesh sensor and the procedure to export the interested data.

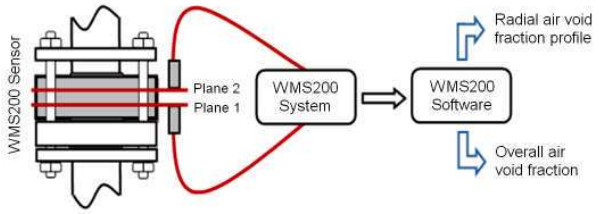

Figure 9: Schematic of the WMS200 measurement.

Like the ERT, the wire-mesh sensor also needs to take reference measurement on the pure water flow. The local void fraction on each crossing point is deduced from the relative difference between the measured voltages of pure water flow (U_w) and the voltages of two phase flow (U_{meas}). Equation 4 shows the single terms involved.

$$\alpha_{air} = \frac{U_W - U_{meas}}{U_W} \quad (4)$$

The FICA ERT can work on the block acquisition mode without on-line displaying the reconstructed images. The maximum frame number acquired at one block is 8000 frames. In this study, 7500 frames were set up for the FICA ERT for one block acquisition, which took approximately 8 seconds. In order to let two modalities run simultaneously, the measurement frequency of WMS was set as 1024 frames per second [18], which was close to the measurement frequency of FICA ERT. 8192 frames were taken from the WMS within 8 seconds. The gain value was set as 15. The calculation of volumetric air void fraction from the measurement data was conducted with the WMS Data Processing Framework 1.4.8.0.

2.2.3. Experiments features

Based on the capability of the flow loop, two flow conditions were examined: bubble flow and slug flow. The various air-water two phase flows are created from the combination of individual air and water feedings, which are shown in Table 2. To avoid the effect of temperature on both the ERT and the WMS, an individual reference was taken after the water flow rate category was changed.

Table 2: Flow rates of air and water

Qa [SLPM]	Qa [m^3/s]	Vsa [m/s]	Qw [RPM]	Qw [m^3/s]	Vsw [m/s]
		BUBBLE	FLOW		
5	8.33E-05	0.042	50	8.02E-04	0.409
10	1.67E-04	0.085	100	1.45E-03	0.740
15	2.50E-04	0.127	145	2.04E-03	1.039
20	3.33E-04	0.169			
25	4.17E-04	0.212			
		SLUG	FLOW		
30	5.00E-04	0.255	20	4.11E-04	0.209
35	5.83E-04	0.296	40	6.72E-04	0.342
40	6.67E-04	0.338	60	9.32E-04	0.475
45	7.50E-04	0.381			
50	8.33E-04	0.423			
55	9.17E-04	0.465			
60	1.00E-03	0.508			
65	1.08E-03	0.550			

Figure 10 represents schematically the concentric ring zones exploited from the ERT and WMS200 systems in order to generate the radial air void fraction profile, where the ring 1 represented the centre of the tube whereas the other concentric circles forms several regions along the cross sectional area of the pipeline investigated (ID=50 mm). The radial void fraction profile represents the averaged value of the void fractions at all the pixel within one corresponding ring.

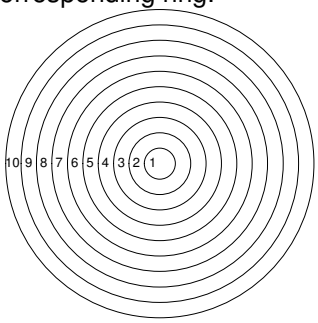

Figure 10: Schematic of the concentric ring zones employed by ERT.

3. Results and discussion

The voltage readings were metered from both WMS 200 and FICA ERT, because two planes of sensors are closer to each other and the flow condition should be the same. Each set of measurement data from ERT and WMS is averaged and extracted to obtain the local air void

fraction profile. This insured a reliable and accurate measuring procedure.

To compare with Figure 3 shown in the section 1.1, the local air void fractions obtained from the WMS are plotted in Figure 11 at a constant water superficial velocity 1.039 m/s with various air superficial velocities. It is evident that the change of the profiles from wall peak to core peak with the increase of the air superficial velocity has the same tendency although the profiles cannot be exactly matched, which may be due to the limited sampling resolution of the WMS and the difference at the pipe diameters between the two experimental set-ups (60 mm in Figure 3 but 50 mm in this research).

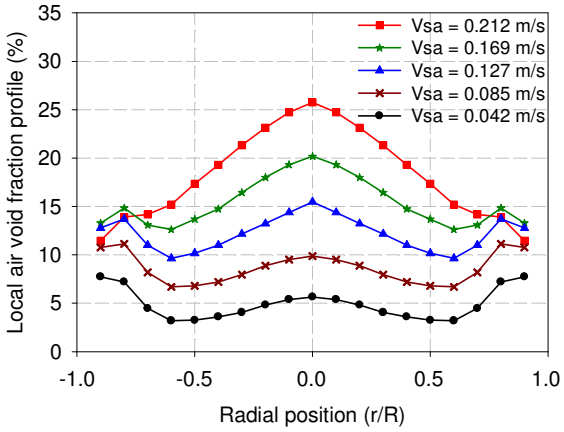

Figure 11: Local air void fraction profiles from WMS, V_{sw} = 1.039 m/s

At the same flow conditions, the local air void fractions obtained from ERT are plotted in Figure 12. It is observed that the details close to pipe wall do not present. The profiles corresponding to low air superficial velocity are also different from those in Figure 3 and Figure 11, which are likely caused by the limits of the back-projection algorithm (SBP) used for image reconstruction. A further comparison between the ERT and the WMS is given below. For simplicity, only the representative local air concentration profiles (Figure 13-Figure 16) are discussed.

On the overall, both instruments meet the predictions, exhibiting higher air concentrations either as the water flow rates decreased or as the air flow rates rose respectively at constant V_{sa} and V_{sw} conditions. Within the bubble flow regime, when the air superficial velocity V_{sa} is kept as 0.085 m/s but the water superficial velocity varies from 0.409 m/s to 1.039 ms.

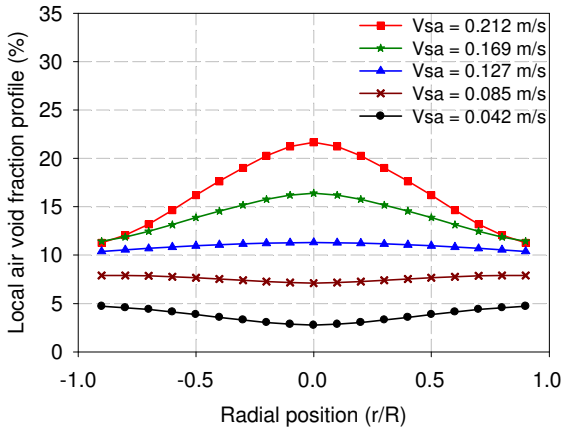

Figure 12: Local air void fraction profiles from ERT, V_{sw} = 1.039 m/s

The air void fraction profiles are shown in Figure 13. The solid curve and dashed curve with different symbols represent the results of WMS and ERT respectively. The void fraction profile of the WMS evolves from the wall peak to the core peak with the decreasing of the water superficial velocity. When the water superficial velocities, V_{sw} are 0.409 m/s and 0.740 m/s, both profiles from the ERT and the WMS have the core peak, with the difference on the centre particularly. However, at high water superficial velocity, V_{sw} = 1.039 m/s, the two profiles have a significant difference. The WMS's profile presents the wall peak format; in contrast, the ERT's profile has a flat shape.

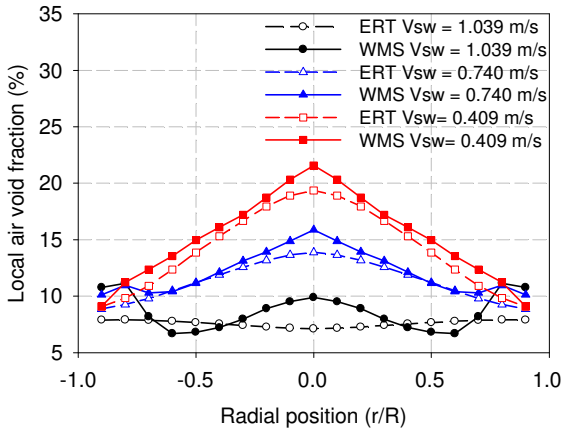

Figure 13: Local air void fraction profiles, V_{sa}=0.085 m/s.

In Figure 14, the water superficial velocity V_{sw} is kept as 0.740 m/s. The wall peak still appears on the WMS's low void fraction profile, generally, the two sets of void fraction profiles have a better agreement at the higher air superficial velocity, V_{sa} = 0.212 m/s.

It is noticed the WMS exhibited wall peak profiles whilst the core peak profiles is generated from the

ERT when the air superficial velocity is 0.042 m/s. The dissimilarity encountered, could be explained due to the insufficient spatial resolution of the ERT by the use of SBP image reconstruction algorithm.

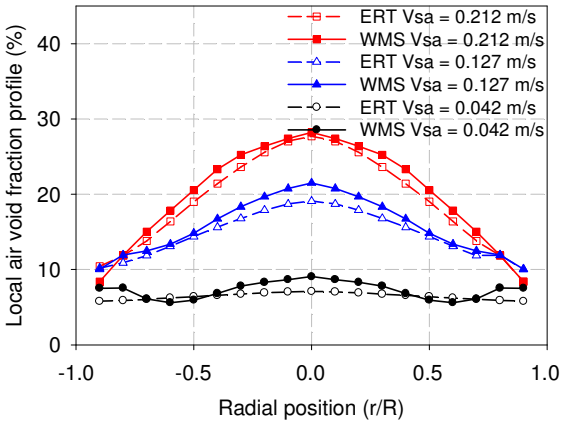

Figure 14: Local air void fraction profiles, V_{sw} = 0.740 m/s.

If the air superficial velocity V_{sa} is kept as 0.465 m/s constant and water superficial velocity varies from 0.209 m/s to 0.475 m/s, the two-phase flow regime changes to the slug flow. The air void fraction profiles shown in Figure 15 demonstrates the clear difference from those in Figure 13. The void fraction values of both WMS and ERT are larger, however, according to the profiles of the WMS, more air evenly distributes in the area within the r/D of ±1.0. The profiles of the ERT remain the typical core peak format. Another finding is the WMS presents larger local void fraction values than the ERT except one or two values close to the pipe wall.

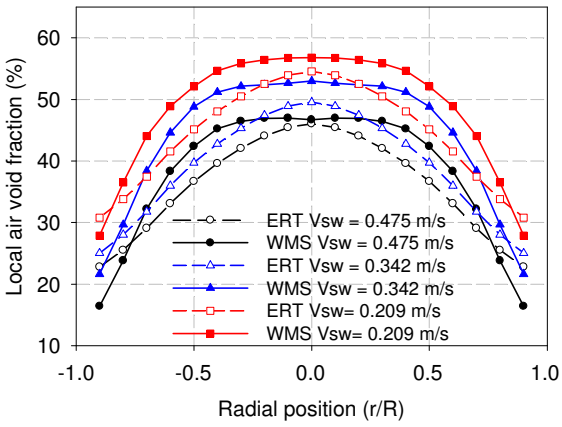

Figure 15: Local air void fraction profiles, V_{sa} = 0.465 m/s.

The similar characteristics of the local air void fraction are maintained in Figure 16, when the water superficial velocity remains 0.342 m/s and the air superficial velocity increases from 0.381 m/s to 0.550 m/s. An offset between the WMS and the ERT exists under each slug flow condition; therefore it is worthwhile to compare the mean air void fraction out of two sensing systems.

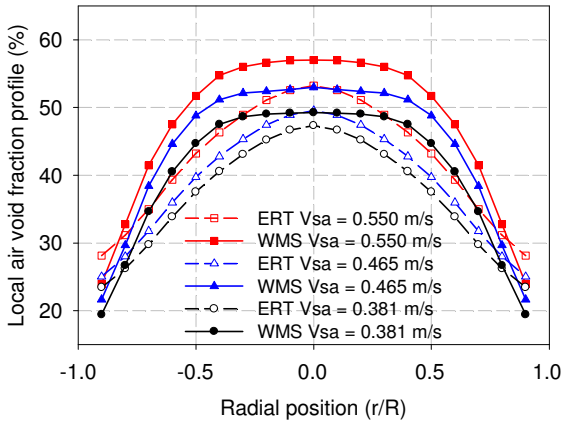

Figure 16: Local air void fraction profiles, V_{sw} = 0.342 m/s.

The mean air void fractions of two flow regimes are displayed in Figure 17. The solid symbols represent the values obtained from the WMS and the hollow symbols represent the values from the ERT. The slug flow has a larger deviation between the ERT and the WMS than that of the bubble flow. And the deviation becomes larger with the increase of the mean void fraction. In addition, the ERT always underestimates the mean void fraction.

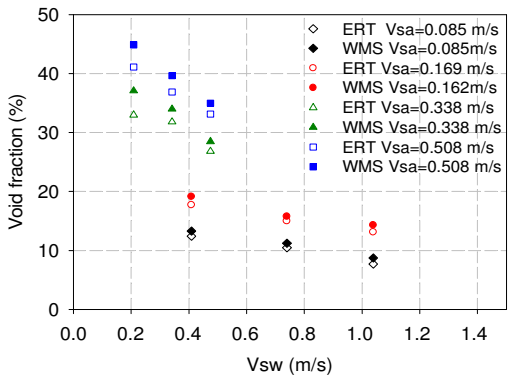

Figure 17: Mean air void fraction of ERT and WMS.

The mean void fractions of ERT and WMS are plotted against each other in Figure 18. It eventually consolidates the finding already encountered above. As shown on the blue triangle points, a good agreement between the two instruments at bubble flow regimes is displayed. However, a gradual discrepancy under slug flow regime is displayed on the red square points. Compared with the WMS, the ERT tends to underestimate the overall air void fraction when over 30%. The deviation between two instruments has a linear relation, which facilitates the calibration for the ERT.

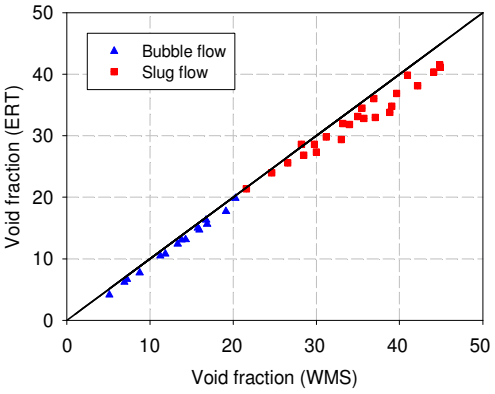

Figure 18: Comparison of overall air void fraction between ERT and WMS.

4. Conclusions

An Electrical Resistance Tomography and a Wire-mesh Sensor were positioned in a vertical pipeline section in order to evaluate the capability of FICA ERT and WMS for metering the dispersed phase distribution and the mean void fraction of the air water two-phase flow. Bubble and Slug flow were hence generated and the following conclusions can be drawn:

- The ERT, with the sensitivity coefficient back-projection image reconstruction algorithm, could not be able to reveal wall peak on the local void fraction profile at low air superficial velocity and high water superficial velocity of the bubble flow, on the contrary, the WMS could. The core peak profiles were obtained from both instruments when the air flow rate was relatively higher.
- The measurement from the ERT and the WMS has a good agreement for the low void fraction (below 30%). Whereas, the ERT tends to underestimate the results with the increase of the void fraction.
- Due to the change of flow regime, the discontinuity of the void fraction profile and the mean void fraction was observed. The results indicated the necessity of using flow regime recognition and model-based correction for flow metering.
- It would be worthy to carry out ERT image reconstructed with other algorithms to improve the measurement precision.
- WMS metering can be used at lower and higher measurement frequency either to validate or discover other possible variation of void fraction profiles encountered.

Acknowledgments

This work was supported by a vacation bursary EPSRC. The authors wish to thank ITS Ltd for its support and guidance throughout the project.

References

[1] MALNES D 1966 Slip ratios and fraction factors in the bubble flow region in vertical tubes - Institute for Atomenergi, Kjeller Research Establishment.

[2] Serizawa A and Kataoka I 1988 Phase Distribution in Two-Phase Flow: Transient Phenomena in Multiphase Flow. *Hemisphere Publishing Corporation*, pp. 179–224.

[3] Wang S K, Lee S J, Jones O C JR and Lahey R T JR 1987, Turbulence structure and phase distribution measurements in bubbly two-phase flow, *Int. J. Multiphase Flow*, 3, 327-343.

[4] Liu T J and Bankoff S G 1993 Structure of air-water bubbly flow in a vertical pipe II. Void fraction, bubble velocity and bubble size distribution, *int J. Heat Mass Translbr.* Vol. 36. No. 4, 1061-1072.

[5] Lahey T J 1990 The analysis of phase separation and phase distribution phenomena using two-fluid models, *Nucl. Eng. Des.*, 2, 17-40.

[6] Seriszawa A et al Dispersed Flow – *Proceeding at the 3rd International Workshop on Two-Phase Flow Fundamentals,* June 15–19, 1992, London, UK.

[7] Lahey R T JR 1988 Turbulence and phase distribution phenomena in two-phase flow: transient phenomena in multiphase flow, *Hemisphere Publishing Corporation*, 139–177.

[8] Lance M and Lopez de Bertodano M 1992 Phase distribution phenomena and wall effects in bubbly two-phase flows - *Proc. of the 3rd Int. Workshop on Two-Phase Flow Fundamentals*, June 15–19, 1992, London, UK.

[9] Prasser H-M Böttger A and Zschau J 1998 A new electrode-mesh tomograph for gas–liquid flows, *Flow Measurement and Instrumentation*, Volume 9, Issue 2, 111-119

[10] Prasser H-M, Misawa M, and Tiseanu I 2005 Comparison between wire-mesh sensor and ultra-fast X-ray tomography for an air–water flow in a vertical pipe, *Flow Measurement and Instrumentation* 16, 73–83.

[11] Prasser H-M, Scholz D and Zippe C 2001 Bubble size measurement using wire-mesh sensors, *Flow Measurement and Instrumentation* 12 (4), 299–312.

[12] Azzopardi B J, Abdulkareem L A, Zhao D, Thiele S, Da Silva M J, Beyer M and Hunt A 2010 Comparison between Electrical Capacitance Tomography and Wire-mesh Sensor Output for Air/Silicone Oil Flow in a Vertical Pipe, *Ind. Eng. Chem. Res., 49,* 8805–8811.

[13] Pietruske H and Prasser H-M 2007 Wire-mesh sensors for high-resolving two-phase flow studies at high pressures and temperatures, *Flow Measurement and Instrumentation*, Volume 18, Issue 2, 87-94

[14] Industrial Tomography Systems LTD 2010 ITS P2+ Electrical Resistance Tomography System - User's Manual, Version 7.0. *Manchester: Industrial Tomography Systems Ltd*.

[15] Industrial Tomography Systems LTD 2010 AIMFlow User's Manual Standard Version 1.0. *Manchester: Industrial Tomography Systems Ltd*.

[16] Wang M, Ma Y, Holliday N, Dai Y, Williams R A and Lucas G 2005 A high performance EIT system, *IEEE Sensors Journal*, 5, 2, 289-299.

[17] Maxwell J C A 1954 Treatise on Electricity and Magnetism, Unabridged Third edition, Vol. 1, *Dover Publications Inc.* New York.

[18] Teletronic Rossendorf GMBH 2009 Wire-mesh Sensor System WMS200 Version 1.2 – User's Manual, *Radeberg, Germany: Teletronic Rossendorf GmbH.*